DEEP LEARNING ON POINT CLOUDS FOR FALSE POSITIVE REDUCTION AT NODULE DETECTION IN CHEST CT SCANS.

Ivan Drokin

Intellogic Limited Liability Company, territory of Skolkovo Innovation Center, 121205, Moscow, Russia ivan.drokin@botkin.ai

Elena Ericheva

Intellogic Limited Liability Company, territory of Skolkovo Innovation Center, 121205, Moscow, Russia elena.ericheva@botkin.ai

May 24, 2022

ABSTRACT

The paper focuses on a novel approach for false-positive reduction (FPR) of nodule candidates in Computer-aided detection (CADe) system after suspicious lesions proposing stage. Unlike common decisions in medical image analysis, the proposed approach considers input data not as 2d or 3d image, but as a point cloud and uses deep learning models for point clouds. We found out that models for point clouds require less memory and are faster on both training and inference than traditional CNN 3D, achieves better performance and does not impose restrictions on the size of the input image, thereby the size of the nodule candidate. We propose an algorithm for transforming 3d CT scan data to point cloud. In some cases, the volume of the nodule candidate can be much smaller than the surrounding context, for example, in the case of subpleural localization of the nodule. Therefore, we developed an algorithm for sampling points from a point cloud constructed from a 3D image of the candidate region. The algorithm guarantees to capture both context and candidate information as part of the point cloud of the nodule candidate. An experiment with creating a dataset from an open LIDC-IDRI database for a feature of the FPR task was accurately designed, set up and described in detail. The data augmentation technique was applied to avoid overfitting and as an upsampling method. Experiments are conducted with PointNet, PointNet++ and DGCNN. We show that the proposed approach outperforms baseline CNN 3D models and demonstrates 85.98 FROC versus 77.26 FROC for baseline models.

1 Introduction

Survival in lung cancer (5 years) is approximately 18.1%¹, which is significantly lower than in other types of cancer since the symptoms of this disease usually appear only when the cancer is already at a late stage. Early-stage lung cancer (stage I) has a five-year survival rate of 60-75%. A recent National Lung Screening Trial (NLST) study has shown that lung cancer mortality can be reduced by at least 20% using a high-risk screening program using low-dose computed tomography (CT) of the chest annually [1]. Computerized tools, especially image analysis and machine learning, are key factors for improving diagnostics, facilitating the identification of results that require treatment, and support the workflow of an expert [2].

CAD systems for computed tomography (CT) typically involve two steps: suspicious lesions (pulmonary nodules candidates) proposing and false positive reduction stage. Although CAD systems have shown improvements in readability by radiologists [3, 4, 5], a significant number of nodules was remained undetected at a low rate of false-positive results, which prohibits the use of CAD in clinical practice. Classification tasks in the medical domain are often a normal vs pathology discrimination task. In this case, it is worth noting the normal class is extremely over-represented in a dataset. Furthermore, it was shown [6] that the nodules have a wide variation in shapes, sizes, and types (for

¹2018 state of lung cancer report: https://www.naaccr.org/2018-state-lung-cancer-report/

example, solid, sub-solid, calcined, pleural, etc.) And most normal training patterns are highly correlated due to the repetitive pattern of normal tissues in each image.

Until recently, CAD systems were built using manually created functions and decision rules. With the advent of a new era of deep learning, the situation has changed. Now, to solve the detection task, CNN models are widely studied. Due to their specificity, CNNs can efficiently work with images and focus on candidate recognition [2]. Due to architectural limitations, convolution networks can proceed with data of a strictly specified size. The size of the input image when incorrectly selected can significantly reduce the effectiveness of the model for objects that are either too large or too small. In this work, we propose a novel approach for the false-positive reduction stage for CAD systems based on point cloud networks. These networks require less memory for training and inference, show more stable results for multiple data sources and, which is the most important, do not impose restrictions on the size of the input image, unlike CNN analogies.

In some cases, the volume of the nodule candidate can be much smaller than the surrounding context, for example, in the case of subpleural localization of the nodule. We propose an algorithm for transforming 3d CT scan data to point cloud.

We developed an algorithm for sampling points from a point cloud constructed from a 3D image of the candidate region. The algorithm must be able to capture both context and candidate information as part of the point cloud of the nodule candidate.

The goal of the false-positive reduction task is to recognize the true pulmonary nodule from the plural candidates, which are received from the detection stage. Since that point cloud sampling method, as well as FPR-model input, strongly depends on segmentation masks suitable for nodule candidates. As well performance evaluation of the FPR is deeply connected with and depends on the performance of a detector. To be sure that the FPR model performance investigated separately from the detector is correct we design and describe full process of receiving of a special artificial dataset for FPR training and evaluation.

2 Previous work

Several articles [7, 8] deal with main concepts of deep learning that are related to the analysis of medical images, and summarize more than 300 articles in this field. The authors consider the use of deep learning for image classification, object detection, segmentation, registration, and other tasks aimed at showing that deep learning methods have spread across the entire field of medical image analysis. The surveys identify problems for the successful application of deep learning for medical imaging tasks as well as appoint specific contributions that solve or circumvent these problems.

As indicated above, currently the based pipeline in the screening task for CAD consists of several stages, the main of which are the detector and the cancer classifier. A two-stage machine learning algorithm is a popular approach that can assess the risk of cancer associated with a CT scan [9, 10, 11, 12, 13]. The first stage uses a nodule detector which identifies nodules contained in the scan. The second step is used to assess whether nodules are malignant or benign.

Methods to solve false positive reduction task separately from full CAD pipeline have been favored a lot recently. A multicontext three-dimensional residual convolutional neural network (3D Res-CNN) was proposed in [14] to reduce false-positive nodules. Using two scales of a network to adapt the variation of pulmonary nodule size, instead of using an unreferenced function concerning the identity mapping, 3D Res-CNN uses a shortcut connection to realize the residual structure. The proposed in [15] a deep 3D residual CNN is much deeper than the traditional 3D CNNs used in medical image processing. Specifically, a spatial pooling and cropping (SPC) layer to extract multi-level contextual information of CT data was designed. An online hard sample selection strategy is applied in the training process to make the network better fit hard samples (e.g., nodules with irregular shapes). The experiments on LUNA16 dataset confirm that their method is robust and that the proposed spatial pooling and cropping layer helps increase the prediction accuracy. The method presented in [16] is based on structure relationship analysis between nodule candidate and vessel, and the modified surface normal overlap descriptor. This approach is leaned on an intuition that a large number of false nodules attached to vessels can be removed by the relationship analysis between nodule candidates and their attached tissues. At the same time, low-contrast nonsolid nodules are separated from the candidates with the modified surface normal overlap descriptor. The algorithm proposed in [17] segments lungs and nodules through a combination of 2D and 3D region growing, thresholding and morphological operations. To reduce the number of false positives, a rule-based classifier is used to eliminate the obvious non-nodules, followed by a multi-view Convolutional Neural Network. The solution achieves a good tradeoff between efficiency and effectivity and saves much computation time. The proposed multi-view 2D network can detect nodules that are isolated, linked to a vessel or attached to the lung wall. The CNN from [18] is fed with nodule candidates obtained by combining three candidate detectors specifically designed for solid, subsolid, and large nodules. For each candidate, a set of 2D patches from differently oriented planes

is extracted. The proposed architecture comprises multiple streams of 2D CNN, for which the outputs are combined using a dedicated fusion method to get the final classification. An evaluation was performed on independent datasets from the LUNA16² and ANODE09³ challenge and DLCST[19].

Recently, several successful works using point clouds in medical image analysis have appeared. In [20] was presented a segmentation of teeth. In [21] segmentation refinement with false positive reduction by point clouds was proposed. In [22] authors use point cloud for vertebra shape analysis.

3 Point Clouds

A point cloud is represented as a set of 3D points $\{P_i|i=1,...,n\}$, where each point P_i is a vector of its (x,y,z) coordinate plus extra feature channels. For semantic segmentation, the input is a single object for part region segmentation, or a sub-volume from a 3D scene for object region segmentation. Input is a subset of points from an Euclidean space and satisfies several properties. It is unordered unlike pixel arrays in images or voxel arrays in volumetric grids. The points are from a space with a distance metric. It means that points are not isolated, and neighboring points form a meaningful subset. As a geometric object, the learned representation of the point set should be invariant to certain transformations. A neural network, named PointNet, was shown in [23]. It directly consumes point clouds, which well respects the permutation invariance of points in the input. Therefore, the model is able to capture local structures from nearby points, and the combinatorial interactions among local structures. The network, provides a unified architecture for applications ranging from object classification, part segmentation, to scene semantic parsing. Though simple, PointNet is highly efficient and effective. Empirically, it shows strong performance on par or even better than state of the art.

Further in [24] authors expand idea with added hierarchical structure to make PointNet be able to capture local structures induced by the metric space points live in, as well as to increase its ability to recognize fine-grained patterns and generalizability to complex scenes. There a discrete metric space $X=(P_i,d)$ is considered as input. The distance metric d defines local neighborhoods that may exhibit different properties. For example, the density and other attributes of points $\{P_i|i=1,...,n\}$ may not be uniform across different locations. Point sets are usually sampled with varying densities, which results in greatly decreased performance for networks trained on uniform densities. While PointNet uses a single max pooling operation to aggregate the whole point set, PointNet++ builds a hierarchical grouping of points and progressively abstract larger and larger local regions along the hierarchy. By exploiting metric space distances, proposed hierarchical PointNet++ is able to learn local features with increasing contextual scales by applying PointNet recursively on a nested partitioning of the input point set. Experiments show that PointNet++ attentively combines features from multiple scales and is able to learn deep point set features efficiently and robust.

Finally, in [25] authors propose a module dubbed EdgeConv suitable for CNN-based high-level tasks on point clouds including classification and segmentation. EdgeConv is differentiable and can be plugged into existing architectures. Instead of working on individual points like PointNet, however, EdgeConv exploits local geometric structures by constructing a local neighborhood graph and applying convolution-like operations on the edges connecting neighboring pairs of points (like in graph neural networks). Proximity in feature space differs from proximity in the input, leading to nonlocal diffusion of information throughout the point cloud. Unlike graph CNNs, EdgeConv graph is not fixed but rather is dynamically updated after each layer of the network. That is, the set of k-nearest neighbors of a point changes from layer to layer of the network and is computed from the sequence of embeddings. In multi-layer systems affinity in feature space EdgeConv captures semantic characteristics over potentially long distances in the original embedding. Extensive evaluation reveals that EdgeConv captures and exploits fine-grained geometric properties of point clouds, compared to existing modules operating largely in extrinsic space or treating each point independently.

4 Data and Processing

It is difficult to directly and objectively compare different CAD systems. In [26], an evaluation system was proposed for the automatic detection of nodules on CT images. A large dataset containing 888 CT scans with annotations from the open LIDC-IDRI database⁴ is available from the NCI Cancer Imaging Archive⁵. A detailed description of the data set is given in [27]. An information about the range of possible patients and disease manifestations as well as data labels receiving process and their quality to support the performance of the method are also represented there. We considered as positive ground truth any nodule noted by at least one radiologist. This increases the number of positive roi in our dataset. In general case this leads to a decrease in the recall at low levels of false positives. Additionally, we took

²LUNA16 challenge homepage: https://luna16.grand-challenge.org/

³ANODE09 challenge homepage: https://anode09.grand-challenge.org/

⁴LIDC-IDRI Dataset: https://wiki.cancerimagingarchive.net/display/Public/LIDC-IDRI

⁵TCIA Collections: https://www.cancerimagingarchive.net

into account all nodule ≤ 3 as a false positive. The motivation for choosing such markup is the goal of constructing a pipeline for detecting nodes with maximum recall, including controversial cases. In our opinion, such borderline situations should be detected by an algorithm, and the doctor will have to make a final decision regarding this region. It is in the controversial and non-obvious cases that the new CAD systems should be of help to the doctor. Since different series in the dataset can have different slice thickness parameters and thus the different distance between slices, we resample series space to 1 mm per voxel side. Full data preprocessing pipeline is showed on Figure 4.

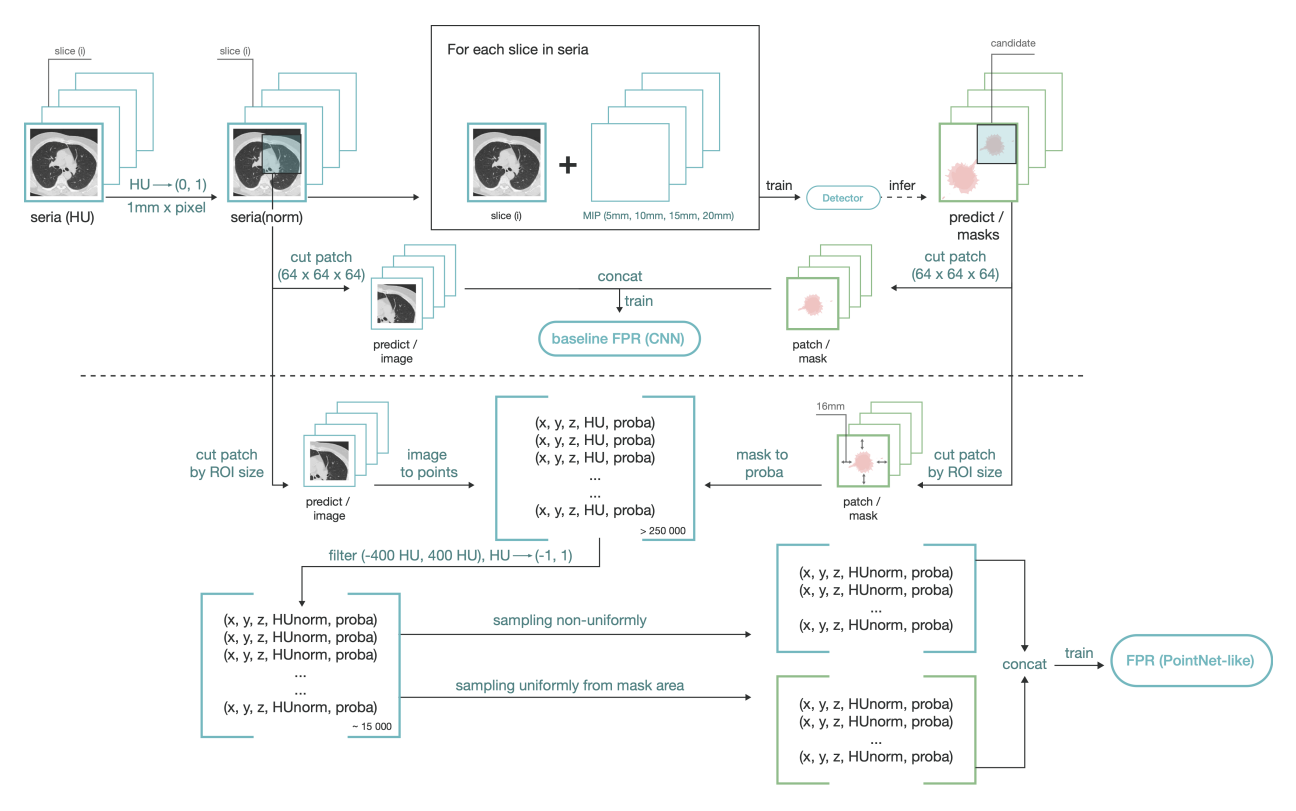


Figure 1: Full pipeline of data processing

4.1 Data Preprocessing for detector

The images are presented on the Hounsfield scale⁶. Voxel intensities are limited to an interval from -1000 to 400 HU and normalized in the range from 0 to 1 (see Equation 1).

$$x_{norm} = \frac{x_{HU} + 1000}{1400} \tag{1}$$

We consider as a detector input full 2D slice concatenated with 4 Maximum Intensity Projection (MIP) images [28] for each sample. MIP images are used by radiologists along with a complete CT exam in order to improve the detection of pulmonary nodules, especially small nodules. MIP images are the superposition of maximum grey values at each coordinate from a stack of consecutive slices. Such a combined image shows morphological structures of isolated nodules and continuous vessels. Experimental results in [28] show that utilizing MIP images can increase the sensitivity and lower the number of false positives, which demonstrates the effectiveness and significance of the proposed MIP-based CNNs framework for automatic pulmonary nodule detection in CT scans. We take MIP images of different slab thicknesses of 5 mm, 10 mm, 15 mm and 20 mm and 1 mm axial section slices as input.

4.2 Collecting a dataset for FPR task

Since our point cloud sampling method, as well as FPR-model input, strongly depends on segmentation masks suitable for nodule candidates, we use the LIDC-IDRI dataset as a source for setting up training and testing data for FPR task. Simple scheme is present on Figure 4.2 We use DenseNet121-TIRAMISU [29] as a detector for nodule candidate

⁶https://en.wikipedia.org/wiki/Hounsfield_scale

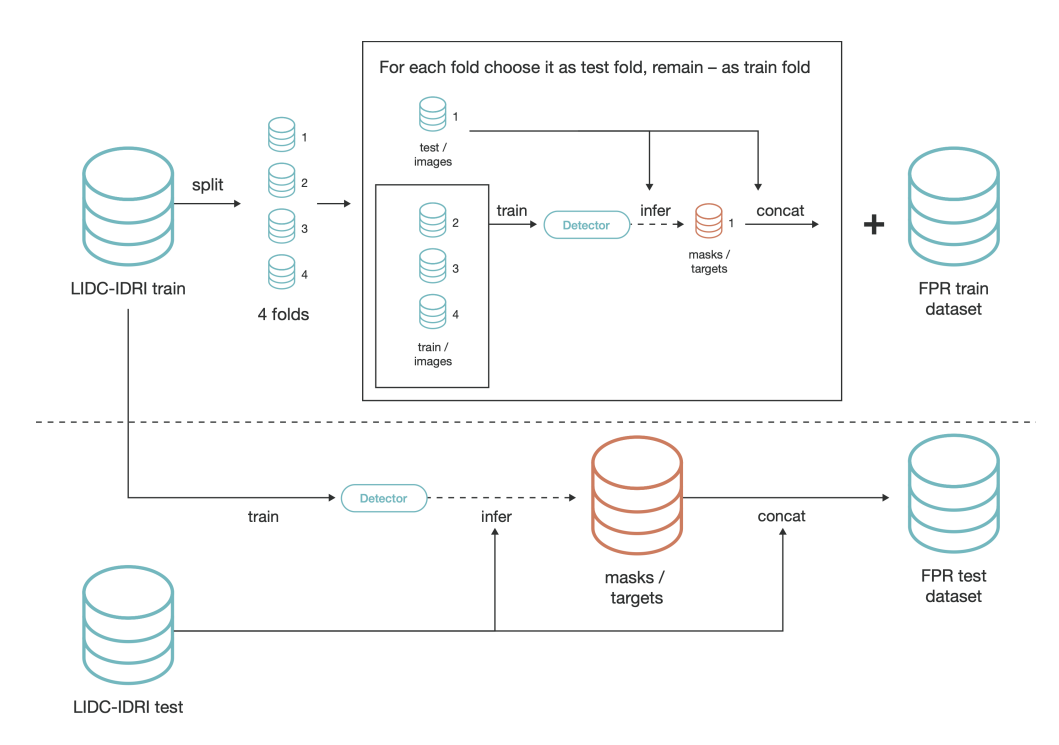


Figure 2: Full scheme of the artificial dataset for FPR task

proposing as well as for train and test dataset for FPR task collection. Firstly, we split LIDC-IDRI dataset on train and test datasets with 75%-25% quotient. For creating of FPR-train dataset we apply 4-fold cross-validation. We consider the LIDC-IDRI train dataset, split it into 4 subsets, train detector on 3 of these subsets, then infer detector on the remaining subset. Then the data received from the infer phase with predicted segmentation masks and probabilities is appended to the training dataset for the FPR task. We repeat this detector train-infer loop 4 times, consistently considering each of 4 fold from LIDC-IDRI as a subset for infer. To create FPR-test dataset we train detector on the full LIDC-IDRI train dataset, then infer detector on the LIDC-IDRI test dataset. The data received from the infer is now considered as a test dataset for the FPR task.

4.3 Data Preprocessing for baseline CNN-like FPR model

For each predicted region of interest (ROI) from the detector network, we cut a patch of the size of $64 \times 64 \times 64$ and the center of which is equal to the center of the segmented nodule area provided by detector. The patch normalized with Equation 1 is considered as an input to the network.

4.4 Data Preprocessing for PointNet-like FPR models

For each predicted region of interest (ROI) from the detector network, we form a bounding box with 16 mm padding. Bounding box here can be any size like a binarized segmenting mask obtained from a detector. Thus we can provide context around candidate and neighborhood with different lung tissues like vessels, pleura, bronchi, etc. Here we got more than 250000 points for further preprocessing, point cloud sampling and using them as model input. To reduce the number of points and exclude the most non-informative points from consideration we select point only with HU value from -400 to 400 from this bounding box. This allows us to catch the vast majority of all nodule types and, at the same time, reduce the number of points to 15000 on average. The input point consists of several features: coordinates of a point, its HU density value, and probability predicted by the detector. As a normalization step, we centered coordinates over the center of the segmented nodule area provided by the detector, as well as translated HU values to (-1,1) interval. The full pipeline scheme of data processing is presented in Figure 4.

4.5 Point Cloud Sampling

For the basis of the proposed point cloud sampling method, we took the method described in the [20]. A naive resampling approach can invoke the loss of important information and is highly application dependent. Since 2016,

several studies investigated point cloud analysis [23, 24] but still applied a uniform resampling for fixing the number of points. Such an approach does not preserve the finer details of data, which is important for the segmentation tasks. Furthermore, it would also miss the existing strong dependency between the label of each point and its location in the point cloud. In [20] authors propose a unique non-uniform resampling mechanism that facilitates the network on a fixed-size resampled point cloud which contains different levels of the spatial resolution, involving both local, fine details and the global shape structure. It is based on the Monte Carlo sampling technique and a Radial Basis Function (*RBF*, Equation 2)

$$RBF(x_i, x_{center}) = exp(-\frac{||x_i - x_{center}||^2}{2\sigma^2})$$
(2)

Let $X \in R^{N*3}$ be a full point cloud with attributes obtained as was described in Subsection 4.4. $x_{center} \in X$ - is a randomly chosen point. Then geometrical similarity (spatial distance) to the point x_{center} can be measured with a weighted distance metric. By resampling, we aim to choose a subset out of X with M points (M < N) that has a dense sampling around the x_{center} and a sparse sampling for farther locations. By randomly drawing (with replacement) a point x_i from the set X, we accept to insert such a point into the target subset only if $RBF > \tau$. The variable τ is a random number from a uniform distribution within the unity interval according to the Monte Carlo technique. σ is a parameter that controls the bandwidth (compactness) of the kernel and depends on candidate radius r.

We introduced two major differences from the method. First, we change σ parameter that controls the bandwidth (compactness) of the kernel and depends on candidate radius r. We choose $\sigma=r/2$. Second, we introduce additional sampling from the nodule area. It should be pointed out that there is a problem of sampling small subpleural candidates with a diameter <5 mm and an overwhelming context around it. The probability of the candidate's point inclusion to the sampled point cloud decreases with the reduction of the candidate's size. To deal with this, we sample additionally with uniform policy only from the area corresponding to the segmenting mask provided by the detector. Thus we can guarantee the appearance of candidate points in the sampled point cloud regardless of the candidate's location or size.

The basic intuition that underlies the proposed sampling method is as follows. The farther the point is from the center of the candidate, the less likely it will be selected in the sampling process. To control this, we introduce sigma as half the candidate radius. Obviously, the farther the point is from the candidate, the less likely it is to be classified as nodule / non-nodule. For example, if the detector incorrectly selected a part of the vessel as a nodule, then the points of interest that are closest to the candidate's points are of greatest interest. This will allow the algorithm to decide that it is a vessel (or bronchus), and not a nodule. Belonging to the candidate is determined by order of the detector by binarizing its mask. All this, on the one hand, guarantees us a context capture regardless of the size of the original candidate. On the other hand, uniform sampling assures us all the necessary information about the region of interest.

4.6 Augmentation techniques

We are dealing with an imbalance between false positives and nodules. In order to avoid overfitting, augmentations are performed on image level as well as on point cloud level. At an image level, Gaussian noise blur and Hounsfield units shift is applied.

$$x'_{HU} = x_{HU} + m_{ijk} * n_{ijk}$$
$$m_{ijk} \sim Poisson(\lambda), n_{ijk} \sim N(0, \sigma)$$

Gaussian noise is added not to a whole slice but to accordance with the random generated mask. In Equation 3, x_{HU} - input image in Hounsfield units and an addendum is a matrix with shape equal image shape. Binary mask m_{ijk} is multiplied with values n_{ijk} sampled from Gauss distribution $N(0,\sigma)$). We use 0.2 for blur appearance probability and interval [0.2, 0.8] for Gaussian filter coefficient. Gaussian filter coefficient alpha is distributed uniformly.

$$x_{inp}' = x_{inp} * (I + \begin{pmatrix} N(0,\sigma) & 0 & \cdots & 0 \\ 0 & N(0,\sigma) & \cdots & 0 \\ \vdots & \vdots & \ddots & \vdots \\ 0 & 0 & \cdots & N(0,\sigma) \end{pmatrix})$$
(3)

At point cloud level we add a rotation (random choice degrees in the transverse planes) and random constant coordination shift. This shift presents compression and extension (Equation 3, where x_{inp} - model's input point cloud, I - is en identity-matrix). Balanced random selection from the data set was applied. Augmentation technique is applied only for training dataset, test data is utilised as is. Augmentation technique is applied both for baseline CNN-like as well as for PointNet-like FPR model.

5 Experiments

5.1 Experiments on LIDC-IDRI

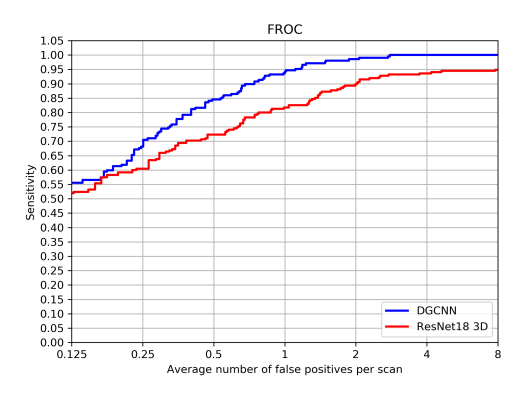


Figure 3: FROC. red: for baseline CNN 3D model and blue: for DGCNN model

The goal of the false-positive reduction task is to recognize the true pulmonary nodule from the plentiful candidates, which is received from the first step of pulmonary nodule candidate detection. Here we investigate FPR performance separately from detector results. We consider the simplest basic architecture of a detector model and use it only as a sampler for creating the FPR train dataset. Performance evaluation of the FPR is deeply connected with and depends on the performance of a detector. That is why we examine FPR performance scoring only on an artificially received dataset as it was described in Section 4.2 and on Figure 4.2

Experiment	0.125 FP	0.25 FP						Mean Sens
Li [30]	0.600	0.674	0.751	0.824	0.850	0.853	0.859	0.773
Liao [31]	0.662	0.746	0.815	0.864	0.902	0.918	0.932	0.834
Baseline	0.514	0.600	0.710					
Pointnet	0.433	0.560	0.693	0.835	0.946	0.977	0.982	0.775
Pointnet w/aug	0.438	0.607	0.698	0.844	0.949	0.990	0.990	0.788
Pointnet++	0.360	0.502	0.640	0.776	0.922	0.972	0.995	0.738
Pointnet++ w/aug	0.356	0.502	0.657	0.789	0.922	0.990	0.995	0.744
DGCNN	0.497	0.628	0.758					
DGCNN w/aug	0.545	0.679	0.842	0.971	0.990	0.995	0.995	0.859

Table 1: Results of the experiments on LIDC-IDRI. Sensitivity per FP level per exam.

We compare several architectures that work with point cloud data with baseline CNN. As the baseline we consider ResNet3D model [32], trained on the same dataset (See Appendix A). We examine 3 PointNet based model: PointNet [23], PointNet++ [24] and DGCNN [25]. We use FROC [33] as the model's quality criterion as a natural metric for nodule detection systems. During experiments, we perform several runs for selected architectures and evaluate model performance with and without augmentations during the training procedure. We use ADAM [34] optimizer with start learning rate 0.001, train models during 70 epochs, decreasing learning rate every 10 epochs twice. We achieve the best FROC 85.98 with the DGCNN model with augmentation. This result outperforms 77.26 FROC for baseline model. Results for all experiments are shown in Table 5.1. At this table, Sens./0.125 FP means that models show sensitivity equal to a number from corresponding table cell at mean 0.125 False Positive per one scan. In the table we also provide modern published results([31], [30]). Our CNN baseline and the PointNet-like approaches have a performance at the level of [30]. In the same time the best DGCNN with augmentation outperforms [31]. Examples of point cloud samples provided in Appendix B.

We added the FROC pictures depending on the nodule size. It shows that in the case with large nodules there is no performance degradation. Even more, PointNet-like models perform better in such cases compare to CNN approach (Figure 4).

To show the effect of the selected sampling method on the performance of the model, we conducted additional experiments with uniform method of sampling. Table 5.1 shows a significant increase in the FROC values for each FP level in case with proposed sampling compare to uniform sampling.

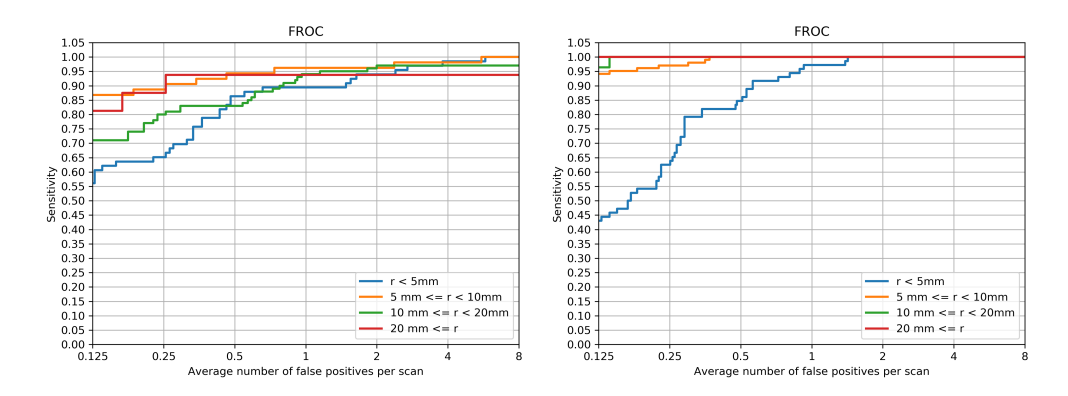


Figure 4: FROC. left: for baseline CNN 3D model and right: for DGCNN model

Table 2: Results of the experiments on LIDC-IDRI. Sensitivity per FP level per exam. Comparison of the performance of FPR models with various point sampling methods.

Experiments DGCNN w/aug	0.125 FP	0.25 FP	0.5 FP	1 FP	2 FP	4 FP	8 FP	Mean Sens
w/uniform sampling	0.36	0.52	0.655	0.78	0.902	0.969	0.99	0.7394
w/(Section 4.5) sampling	0.545	0.679	0.842	0.971	0.990	0.995	0.995	0.859

5.2 Experiments on LUNA2016 nodule detector track. Benchmark

Table 3: Results of the experiments on LUNA nodule detection track. Sensitivity per FP level per exam

Experiment	0.125 FP	0.25 FP	0.5 FP	1 FP	2 FP	4 FP	8 FP	Mean Sens
Gupta [35]	0.531	0.629	0.790	0.835	0.843	0.848	0.856	0.763
Hamidian [36]	0.583	0.687	0.742	0.828	0.886	0.918	0.933	0.797
Xie [37]	0.734	0.744	0.763	0.796	0.824	0.832	0.834	0.790
Liao [31]	0.662	0.746	0.815	0.864	0.902	0.918	0.932	0.834
Dou [38]	0.659	0.745	0.819	0.865	0.906	0.933	0.946	0.839
Zhu [39]	0.692	0.769	0.824	0.865	0.893	0.917	0.933	0.842
Li [30]	0.739	0.803	0.858	0.888	0.907	0.916	0.920	0.862
Wang [40]	0.676	0.776	0.879	0.949	0.958	0.958	0.958	0.878
Ding [41]	0.748	0.853	0.887	0.922	0.938	0.944	0.946	0.891
Khosravan [42]	0.709	0.836	0.921	0.953	0.953	0.953	0.953	0.897
Ozdemir [43]	0.832	0.879	0.920	0.942	0.951	0.959	0.964	0.921
Cao [44]	0.848	0.899	0.925	0.936	0.949	0.957	0.960	0.925
Baseline	0.686	0.811	0.840	0.929	0.972	0.972	0.972	0.883
DGCNN w/aug	0.725	0.832	0.901	0.933	0.945	0.945	0.945	0.8894

The generally accepted benchmark for the FPR task in nodule detection is the LUNA2016 FPR track competition. We believe that comparison the results with the existing benchmark is important for a more transparent reflection of the results obtained and the performance of the model. But it is also necessary to note that we cannot use the LUNA2016 FPR track data as a benchmark for the point cloud based model. Because of the data on this track does not have the necessary markup. Our FPR model inputs strongly depend on segmentation masks suitable for nodule candidates(see Section 4.2).

Nevertheless, we can evaluate the entire pipeline on the LUNA2016 nodule detection track. We are aware of the strong dependence of the evaluation of the whole pipeline on the performance of the detector. FNs cannot be recovered by the FPR model. A weak detector can create many FNs. We want to additionally note the study of the performance of the detector is beyond the scope of this work. Nevertheless, for a more transparent estimation of the FPR models, we briefly present the results of the detector performance the LUNA2016 nodule detection track: mean sensitivity 0.4132, max recall 0.9776 achieved on 43 FP per case.

The Table 5.2 shows that both the CNN baseline and the PointNet approaches in conjunction with a weak detector have a performance at the level of modern published results.

6 Ablation study

As part of the formulation of the general objective of this work — testing the hypothesis that lung nodules can be effectively represented as a point cloud — we decided that it would be interesting to bring the results of an ablation study. The problem clarification: patch classification refers to the classification of objects presented on these patches the nodule is represented there or not. Common false-positive detections are pieces of bronchi, blood vessels, fibrosis, etc. In the task of separating these objects from the nodules, information about their shape is critical. And by the way, therefore, coordinates are needed as data for representation. The coordinates contain information about the shape of the object represented on the patch. Coordinates "structure" points in a point cloud. Speaking more formally, we propose to present objects not as a 3D image, but as a list of points with their characteristics. The most obvious characteristic of a point is their coordinates (x,y,z). We can expand this list by adding information about the radiological density (HU) and probability of the detector (p). Thus, each example is represented as a list $(x_i, y_i, z_i, hu_i, p_i)i = 1...n$, where n is the number of points in the example. And already this data is used by the model as an input. The results presented in the Table 6 confirm our assumptions about the importance of HU and p in the context of solving the FPR problem based on PointNet-like models and presenting samples in the point cloud. Results of such an experiment show that coordinate information for each point is essential for success nodule/non-nodule classification. This result is consistent with our hypotheses and assumptions.

Table 4: Results of the experiments on LIDC-IDRI. Sensitivity per FP level per exam. Comparison of the performance of FPR models with various point point representation in the Point Cloud.

Experiment	0.125 FP							Mean Sens
Li [30]	0.600	0.674	0.751	0.824	0.850	0.853	0.859	0.773
Liao [31]	0.662		0.815					
Baseline	0.514	0.600	0.710	0.812	0.893	0.931	0.944	0.772
DGCNN (xyz + HU + p)	0.545	0.679	0.842					
DGCNN (xyz + p)	0.382	0.577	0.756	0.902	0.959	0.979	0.992	0.792
DGCNN (xyz + HU)	0.362	0.467	0.630	0.764	0.862	0.979	0.995	0.723
DGCNN (xyz)	0.362	0.451	0.528	0.646	0.829	0.947	0.995	0.680
DGCNN (HU + P)	0.121	0.211	0.308	0.410	0.597	0.845	0.983	0.496

6.1 Conclusion and Discussion

We propose a novel approach for solving False-Positive Reduction task for lung nodule detection CAD systems based on the representation of nodule candidate as a set of points with known coordinates, radiodensity, and class probability, predicted by a detector. Such representation allows us to use a wide set of models designed to work with point cloud and graph data. Representation of lung tissue as a set of points is quite efficient: a major part of a lung volume is air and observation of it can be skipped without missing any important information. This leads us to much more lightweight models compared to traditional CNN 3D, including the usage of the entire patch extracted from CT scan.

We provide an extensive comparison with sota results from open sources. For FPR task we compare PointNet-like aproaches with widely popular CNN-like models. We have shown that DGCNN model can outperform CNN 3D at False Positive reduction task. We also provide an ablation study as essential for the paper and understanding of the method of the use of point clouds. The results show the importance of such parameters as radiology density HU and detector probability p in the context of presenting samples in the point cloud.

We also present augmentation techniques that lead to a better model performance. According to this results we assume that such representation and approach can be successfully transferred to nodule detection task and we plan to extend this work and build the pipeline for nodule detection on point cloud representation on chest CT scans entirely. Another major question for further research is testing on other datasets from different sources.

References

[1] D. Aberle and et al. Reduced lung-cancer mortality with low-dose computed tomographic screening. *The New England Journal of Medicine*, 365:395–409, 2011.

- [2] H. Greenspan, B. van Ginneken, and R. Summers. Guest editorial deep learning in medical imaging: Overview and future promise of an exciting new technique. *IEEE Transactions on Medical Imaging*, 35:1153–1159, May 2016.
- [3] B. Sahiner and et al. Effect of cad on radiologists' detection of lung nodules on thoracic ct scans: Analysis of an observer performance study by nodule size. *Academic Radiology*, 2010.
- [4] N. Wu and et al. Deep neural networks improve radiologists' performance in breast cancer screening. *IEEE Transactions on Medical Imaging*, 2019.
- [5] D. Wang, A. Khosla, R. Gargeya, H. Irshad, and A. Beck. Deep learning for identifying metastatic breast cancer. *arXiv:1606.05718*, 2016.
- [6] A. Arindra and A. Setio. Pulmonary nodule detection in ct images: False positive reduction using multi-view convolutional networks. *IEEE Transaction on Medical Imaging*, 35(5), May 2016.
- [7] G. Litjens and et al. A survey on deep learning in medical image analysis. *Medical Image Analysis*, 42:60–88, 2017.
- [8] D. Ravì and et al. Deep learning for health informatics. *IEEE Journal of Biomedical and Health Informatics*, PP, 12 2016.
- [9] S. Trajanovski and et al. Towards radiologist-level cancer risk assessment in ct lung screening using deep learning. *arXiv:1804.01901*, 2018.
- [10] K. He, X. Zhang, S. Ren, and J. Sun. Deep residual learning for image recognition. *IEEE Conference on Computer Vision and Pattern Recognition (CVPR)*, pages 770–778, 2016.
- [11] H. Tang, C. Zhang, and X. Xie. Nodulenet: Decoupled false positive reduction for pulmonary nodule detection and segmentation. *The Medical Image Computing and Computer Assisted Intervention (MICCAI)*, pages 266–274, 10 2019.
- [12] H. Tang, X. Liu, and X. Xie. An end-to-end framework for integrated pulmonary nodule detection and false positive reduction. *IEEE 16th International Symposium on Biomedical Imaging (ISBI)*, 03 2019.
- [13] A. Hunar and M. Sozan. A deep learning technique for lung nodule classification based on false positive reduction. *Journal of Zankoy Sulaimani Part A*, 21:107–116, 06 2019.
- [14] Z. Zhang, X. Li, Q. You, and X. Luo. Multicontext 3d residual cnn for false positive reduction of pulmonary nodule detection. *International Journal of Imaging Systems and Technology*, 29, 12 2018.
- [15] H. Jin, Z. Li, R. Tong, and L. Lin. A deep 3d residual cnn for false positive reduction in pulmonary nodule detection. *Medical Physics*, 45, 03 2018.
- [16] G. Cao, Y. Liu, and K. Suzuki. A new method for false-positive reduction in detection of lung nodules in ct images. *International Conference on Digital Signal Processing*, DSP, 2014:474–479, 08 2014.
- [17] S. El-Regaily, M. Salem, M. Aziz, and M. Roushdy. Multi-view convolutional neural network for lung nodule false positive reduction. *Expert Systems with Applications*, 10 2019.
- [18] A. Setio and et al. Pulmonary nodule detection in ct images: false positive reduction using multi-view convolutional networks. *IEEE Transactions on Medical Imaging*, 2016.
- [19] P. Jesper and et al. The danish randomized lung cancer ct screening trial—overall design and results of the prevalence round. *Journal of thoracic oncology: official publication of the International Association for the Study of Lung Cancer*, 4:608–14, 05 2009.
- [20] F. Zanjani and et al. Deep learning approach to semantic segmentation in 3d point cloud intra-oral scans of teeth. *Proceedings of The 2nd International Conference on Medical Imaging with Deep Learning*, 102:557–571, 08–10 Jul 2019.
- [21] F. Balsiger, Y. Soom, O. Scheidegger, and M. Reyes. Learning shape representation on sparse point clouds for volumetric image segmentation. *The Medical Image Computing and Computer Assisted Intervention (MICCAI)*, 11765, 2019.
- [22] A. Sekuboyina and et al. Probabilistic point cloud reconstructions for vertebral shape analysis. *The Medical Image Computing and Computer Assisted Intervention (MICCAI)*, 11769, 2019.
- [23] C. Qi, H. Su, K. Mo, and L. Guibas. Pointnet: Deep learning on point sets for 3d classification and segmentation. 2017 IEEE Conference on Computer Vision and Pattern Recognition (CVPR), pages 77–85, 2016.
- [24] C. Qi, L. Yi, H. Su, and L. Guibas. Pointnet++: Deep hierarchical feature learning on point sets in a metric space. *NIPS*, 2017.

- [25] Y. Wang and et al. Dynamic graph cnn for learning on point clouds. ACM Transactions on Graphics, 38, 01 2018.
- [26] S. Armato and et al. The lung image database consortium (lidc) and image database resource initiative (idri): a completed reference database of lung nodules on ct scans. *Medical Physics*, 38:915–931, 2011.
- [27] C. Jacobs and et al. Computer-aided detection of pulmonary nodules: a comparative study using the public lide/idri database. *European Radiology*, 2016.
- [28] Z. Sunyi and et al. Automatic pulmonary nodule detection in ct scans using convolutional neural networks based on maximum intensity projection. *IEEE Transactions on Medical Imaging*, PP:1–1, 08 2019.
- [29] S. Jégou, M. Drozdzal, D. Vazquez, A. Romero, and Y. Bengio. The one hundred layers tiramisu: Fully convolutional densenets for semantic segmentation. *arXiv:1611.09326*, 2016.
- [30] Y. Li and Y. Fan. Deepseed: 3d squeeze-and-excitation encoder-decoder convnets for pulmonary nodule detection. *arXiv*:1904.03501, 04 2019.
- [31] F. Liao and et al. Evaluate the malignancy of pulmonary nodules using the 3-d deep leaky noisy-or network. *IEEE Transactions on Neural Networks and Learning Systems*, 30:3484–3495, 2019.
- [32] K. He, X. Zhang, S. Ren, and J. Sun. Deep residual learning for image recognition. 2016 IEEE Conference on Computer Vision and Pattern Recognition (CVPR), pages 770–778, 2016.
- [33] A. Bandos, H. Rockette, T. Song, and D. Gur. Area under the free-response roc curve (froc) and a related summary index. *Biometrics*, 65(1):247–256, 2009.
- [34] D. Kingma and J. Ba. Adam: A method for stochastic optimization. *International Conference on Learning Representations*, 12 2014.
- [35] A. Gupta, T. Saar, O. Martens, and Y. Moullec. Automatic detection of multisize pulmonary nodules in ct images: Large-scale validation of the false-positive reduction step. *Medical Physics*, pages 1135–1149, 01 2018.
- [36] S. Hamidian, B. Sahiner, N. Petrick, and A. Pezeshk. 3d convolutional neural network for automatic detection of lung nodules in chest ct. *Proceedings of SPIE-the International Society for Optical Engineering*, 10134:1013409, 03 2017.
- [37] H. Xie, D. Yang, N. Sun, Z. Chen, and Y. Zhang. Automated pulmonary nodule detection in ct images using deep convolutional neural networks. *Pattern Recognition*, 85:109–119, 2019.
- [38] Q. Dou, H. Chen, Y. Jin, H. Lin, J. Qin, and P.-A. Heng. Automated pulmonary nodule detection via 3d convnets with online sample filtering and hybrid-loss residual learning. *The Medical Image Computing and Computer Assisted Intervention (MICCAI)*, pages 630–638, 09 2017.
- [39] W. Zhu and et al. Deeplung: Deep 3d dual path nets for automated pulmonary nodule detection and classification. *IEEE WACV*, page 673–681, 01 2018.
- [40] B. Wang, G. Qi, S. Tang, L. Zhang, L. Deng, and Y. Zhang. Automated pulmonary nodule detection: High sensitivity with few candidates. *21st International Conference, Proceedings, Part II*, pages 759–767, 09 2018.
- [41] J. Ding, A. Li, Z. Hu, and L. Wang. Accurate pulmonary nodule detection in computed tomography images using deep convolutional neural networks. *The Medical Image Computing and Computer Assisted Intervention (MICCAI)*, pages 559–567, 2017.
- [42] N. Khosravan and U. Bagci. S4nd: Single-shot single-scale lung nodule detection. *The Medical Image Computing and Computer Assisted Intervention (MICCAI)*, pages 794–802, 05 2018.
- [43] O. Ozdemir, R. Russell, and A. Berlin. A 3d probabilistic deep learning system for detection and diagnosis of lung cancer using low-dose ct scans. *IEEE Transactions on Medical Imaging*, PP:1–1, 10 2019.
- [44] H. Cao and et al. Two-stage convolutional neural network architecture for lung nodule detection. *IEEE Journal of Biomedical and Health Informatics*, 01 2020.

A ResNet3D details

We use modified ResNet18 as the baseline. We change all convolution layers to 3d convolutions and add two additional hidden fully connected layers after global average pooling with batch normalization and ReLU activation. As the final activation we use a sigmoid function (see details at Figure 5). We use Adam optimizer with the initial learning rate equal to 0.001, train model during 75 epochs and decrease learning rate twice with every 10 epochs. We also add Gaussian blur, flips and random rotation as augmentation techniques. We balance dataset out by upsampling all positive candidates so positive and negative candidates ratios are equal to each other.

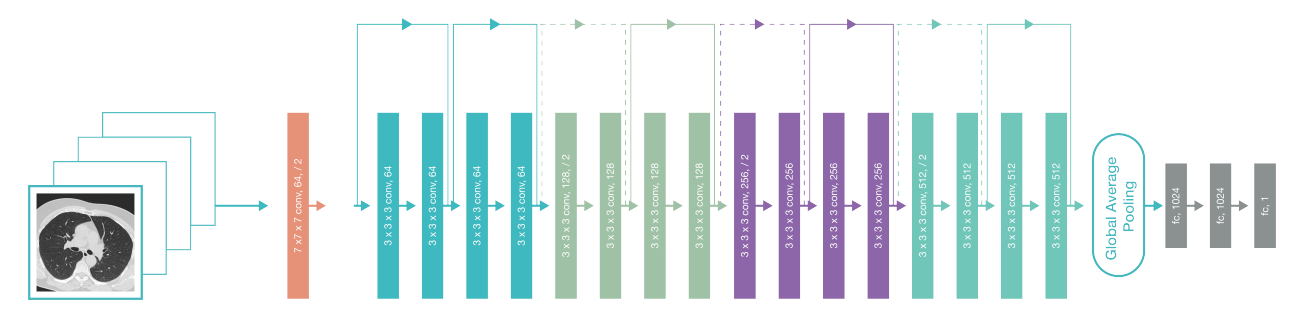


Figure 5: Examples of point cloud samples for negative candidates

B Point Cloud samples visualisation

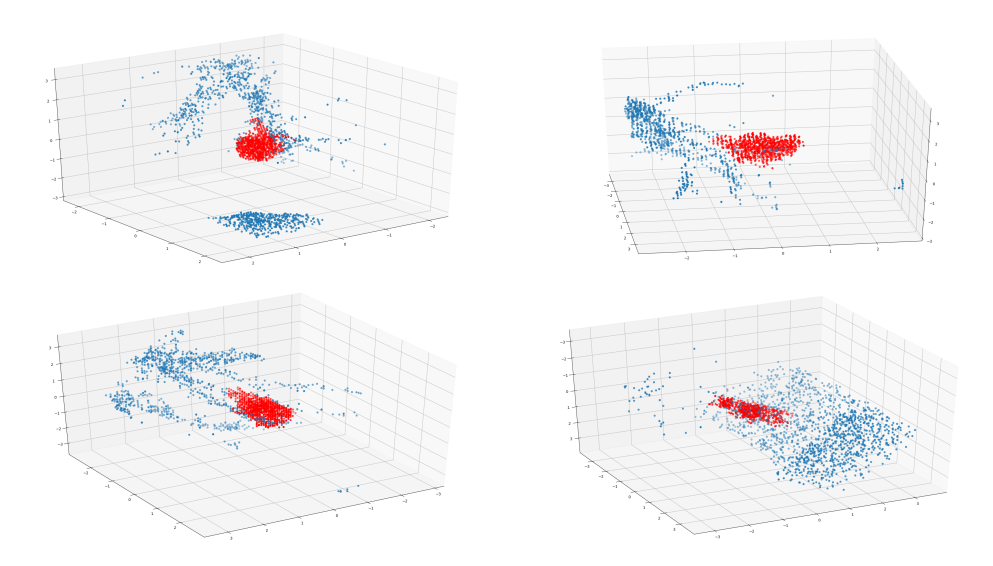


Figure 6: Examples of point cloud samples for positive candidates

At Figure 6 and Figure 7 red points signify those points that detector marked as nodule candidates. Blue points represent the background. These plots show that point cloud contains all necessary information for successful separation of true positive candidates from false-positive candidates.

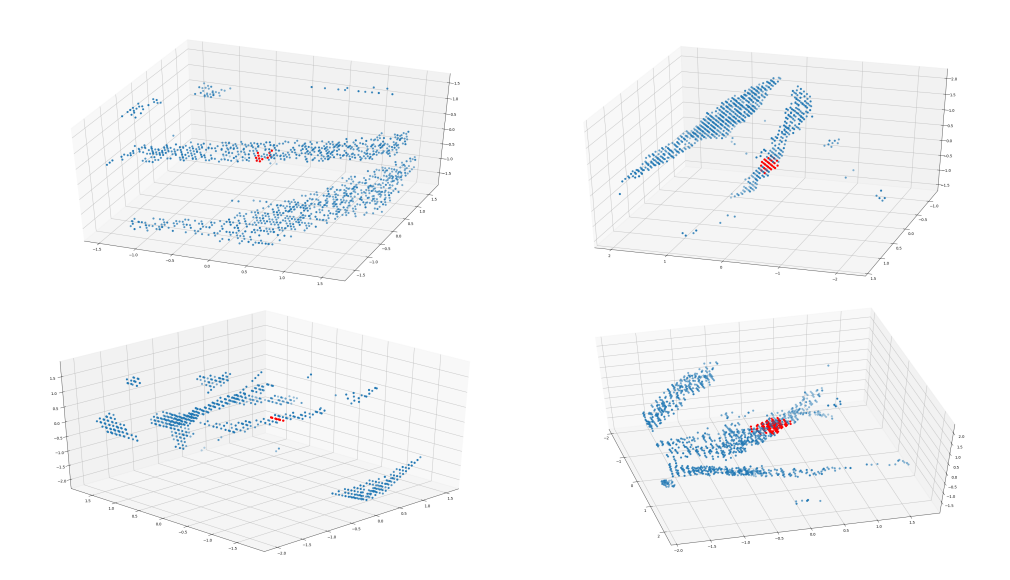


Figure 7: Examples of point cloud samples for negative candidates